ACS OMEGA

Open Access

This article is licensed under CC-BY-NC-ND 4.0

http://pubs.acs.org/journal/acsodf

Article

Biogenic Vaterite Calcium Carbonate-Silver/Poly(Vinyl Alcohol) Film for Wound Dressing

Mohammad Hossein Azarian, Tiraporn Junyusen, and Wimonlak Sutapun*

Cite This: *ACS Omega* 2024, 9, 955−969

Read Online

ACCESS | Metrics & More | Article Recommendations

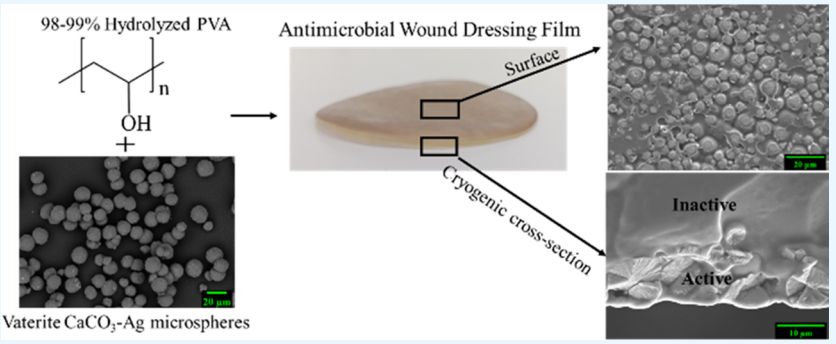

ABSTRACT: Vaterite, a spherical polymorph of $CaCO_3$, shows potential as a carrier for the stable and controlled release of silver nanoparticles (AgNPs), preventing their aggregation or loss of efficacy during application. Furthermore, the embedding of $CaCO_3$−Ag in a poly(vinyl alcohol) (PVA) matrix helps effectively encapsulate and protect the $CaCO_3$−Ag microspheres and provides mechanical stability for better contact with the wound surface. This article focuses on the fabrication of an antimicrobial and biocompatible absorbent film embedded with precipitated biogenic vaterite $CaCO_3$−Ag microspheres. The impact of vaterite $CaCO_3$−Ag on the physical, chemical, nanomechanical, biocompatibility, and antimicrobial properties of the PVA films was investigated. The morphology study revealed a bilayer film structure with an inactive and active surface containing homogeneously distributed vaterite $CaCO_3$−Ag. The X-ray photoelectron spectroscopy (XPS) analysis of the spin−orbit splitting in the Ag $3d_{5/2}$ and Ag $3d_{3/2}$ peaks indicated the presence of both metallic and ionic states of silver in vaterite $CaCO_3$−Ag prior to its incorporation into the PVA polymer matrix. However, upon embedding in the PVA matrix, a subsequent transformation to solely ionic states was observed. The nanomechanical properties of PVA improved, and the reduced modulus and hardness increased to 14.62 ± 5.23 and 0.64 ± 0.29 GPa, respectively. The films demonstrate a significant activity toward Gram-negative *Escherichia coli* bacteria. The release of AgNPs was studied in both open and closed systems at pH 6, mimicking the pH environment of the wound, and it demonstrated a dependency on the type of capping agent used for synthesis and loading of AgNPs. The results further revealed the biocompatibility of the prepared films with human dermal fibroblast cells at a concentration of ≤5 mg/mL, making them applicable and functional for wound dressing applications.

1. INTRODUCTION

Biocompatible absorbent materials derived from the combination of inorganic and organic components are highly desirable to be employed in biomedical, food industry, and pharmaceutical applications due to their high water absorption capacity, biodegradability, and mechanical stability. However, their ability to hold a large quantity of water may facilitate bacterial growth and consequently increase the chance of infection.[1] Diseases derived from bacterial infections are a serious human health threat, specifically in *Carbapenem-Resistant Enterobacteriaceae* (CRE) bacteria groups, which nearly become resistant to all available antibiotics.[2] Therefore, simply incorporating the antibiotic drugs into an absorbent film is not an ideal option due to the emergence of antibiotic resistance in pathogenic microbes. An alternative and more effective way is to use metal nanoparticles such as zinc,[3,4] silver,[5,6] gold,[7] and copper[8−10] as a potential solution to solve the global antibiotic resistance.[11] Despite the various proposed and adopted antibacterial mechanisms of metal nanoparticles, their explicit mechanisms are still dubious and unclear. However, as metal nanoparticles do not bind to a specific receptor in the bacterial cell, the bacteria are unable to develop any resistance.[12]

Received: September 18, 2023
Revised: October 27, 2023
Accepted: November 22, 2023
Published: December 19, 2023

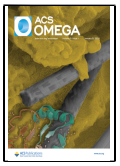

© 2023 The Authors. Published by American Chemical Society

For wound dressing application, Shalmun et al.[13] incorporated ZnO within a sodium alginate (SA)/poly(vinyl alcohol)-(PVA) film as a potential biomaterial and showed that the prepared films have antimicrobial activity against *Staphylococcus aureus* and *Escherichia coli* bacteria. In another study, Jin et al.[14] produced a nanofibrous scaffold consisting of poly(L-lactic acid)-*co*-poly(ε-caprolactone) loaded with AgNP films and showed that human skin fibroblasts cultured on the scaffolds possess better cell proliferation with 0.25 wt % AgNPs having antibacterial activity against both Gram-positive and Gram-negative bacteria.

Silver remains the best option among the widely used metal nanoparticles due to its superior antimicrobial, anti-inflammatory, and antioxidative properties as well as ease of preparation.[15] Silver-loaded wound dressing films have already established a presence in the market,[16−18] but researchers and scientists continue to search for new and innovative combinations between silver and different polymer matrices. The results of these efforts have been highly encouraging and hold great promise for the future of wound care treatments. The use of silver in wound dressings provides excellent antimicrobial properties and helps prevent the growth of harmful bacteria. By incorporation of new materials and techniques, the potential for even more effective wound dressings is on the horizon. Recently, Ueda et al.[19] reported the preparation of calcite calcium carbonate powders loaded with AgNPs by ultrasonic spray-pyrolysis (USSP) of calcium acetate in silver colloid in an attempt to serve as a novel antibacterial inorganic filler material and showed that calcium carbonate could facilitate the effective release of Ag^+ ions for over 28 days. However, a more eco-friendly and sustainable way to obtain calcium carbonate powders with desirable polymorphs would be from discarded eggshells proposed in this research. Eggshells comprise more than 97 wt % biogenic calcium carbonates in calcite polymorph structures.[20] However, due to its cubic structure, the calcite polymorph is unsuitable as a delivery vehicle. The calcite structure of eggshell calcium carbonate with a cubical morphology may transform into a spherical vaterite polymorph structure by precipitation. The precipitation technique offers control over the formation of vaterite $CaCO_3$ microspheres, with the potential to adjust process parameters such as pH and salt molar concentration. These adjustments enable the attainment of the desired particle size, morphology, and formation of specific polymorphs.[21,22] The vaterite $CaCO_3$ can serve as a delivery vehicle due to its spherical morphology and high biocompatibility. The advantage of $CaCO_3$−Ag in biomedical applications lies in its potential to provide the controlled and stable release of silver nanoparticles, enhancing antimicrobial efficacy while maintaining biocompatibility.[23,24]

Wound dressing materials are engineered to aid natural healing by guarding the wounds against external contaminants. However, the ideal wound dressing must have several crucial properties to ensure efficient healing and patient comfort. These properties include biocompatibility, allowing for harm-free integration with the patient's skin and body; high water absorption capacity, to effectively manage excess fluid and prevent infection; biodegradability, to reduce waste and minimize harm to the environment; mechanical stability, to withstand physical stress and provide adequate protection; and finally, antimicrobial activities, to prevent the growth of harmful bacteria and other microorganisms.[25,26] Therefore, the material properties of polymeric films must meet certain requirements.

Various natural or synthetic biocompatible polymers were embedded with nanoparticles and have been reported so far for skin tissue engineering scaffolds such as poly(acrylic acid) (PAA),[27] chitosan,[28,29] poly(L-lactic acid),[30] collagen,[31] hyaluronic acid (HA),[32] gelatin,[33] polycaprolactone (PCL),[34] PVA,[35,36] etc. Out of these, PVA is the most studied macromolecule for biomedical applications due to its level of biodegradability, mechanical properties, and excellent biocompatibility.[37,38] Jinag et al.,[39] for instance, have demonstrated that the PVA hydrogel has a similar microstructure to the porcine liver and therefore is a promising biomaterial suitable for tissue-mimicking, vascular cell culturing, and vascular implanting. In a similar study, Augustine et al.[40] prepared a PVA membrane containing green synthesized AgNPs for wound dressing applications. They showed that the obtained membranes possess good mechanical strength, excellent exudate uptake capacity, antibacterial activity against both Gram-negative and Gram-positive bacteria, blood compatibility, and cytocompatibility. More recently, Guo et al.[41] incorporated AgNPs into PVA blended with chitosan for wound dressing and showed that the hydrogel films have remarkable mechanical stability and resist external damage. It also exhibits effective antibacterial properties against *S. aureus* and *E. coli* and demonstrates good biocompatibility without any cytotoxicity.

This work aims to produce antimicrobial and biocompatible polymer films embedded with precipitated biogenic vaterite $CaCO_3$−Ag for wound dressing applications. The embedded PVA films were characterized with respect to their spectroscopic, structural, thermal, mechanical, morphological, antimicrobial, and cytotoxicity properties. Embedding vaterite $CaCO_3$−Ag in PVA macromolecules maintains the AgNPs' stability and functionality and protects them from environmental exposure. The combination of vaterite $CaCO_3$ as a carrier and stabilizer for AgNPs, along with the mechanical stability, controlled release capability, biocompatibility, and high water absorption capacity offered by the PVA film, contributes to the overall effectiveness of using these materials for advanced wound healing.

2. EXPERIMENTAL DETAILS

2.1. Materials. Chicken eggshell wastes were obtained from a local bakery shop near the Suranree University of Technology (SUT) in Thailand, Nakhon Ratchasima. The eggshells were washed with water and boiled for 6 h at 100 °C to remove the eggshell membranes and organic residues. The eggshells were ground to a fine powder after being dried at 60 °C for 24 h. Silver nitrate (99.0%, ACS reagent), sodium carbonate (powder, 99.5%, ACS reagent), sodium carboxymethyl cellulose (CMC, average M_w of 90,000 g mol^{-1}, powder), and poly(sodium 4-styrenesulfonate) (PSS, average M_w of 70,000 g mol^{-1}, powder) were obtained from Sigma-Aldrich. Poly(vinyl alcohol) (PVA, 98−99% hydrolyzed, high molecular weight) was purchased from Alfa Aesar. Nitric acid 65% (AR grade, M_w of 63.01 g mol^{-1}) was purchased from ANaPURE.

2.2. One-Pot Synthesis of Vaterite $CaCO_3$−Ag Microspheres. The polyelectrolyte solution was prepared at ambient temperature by dissolving 0.5 g of CMC or PSS in 20 mL of deionized (DI) water. After the complete dissolution of polyelectrolyte, 0.01 M silver nitrate solution was prepared separately in 5 mL of DI water. The stable silver colloid was prepared by adding 0.01 M silver nitrate solution to the polyelectrolyte solution under stirring at ambient temperature. The calcium nitrate solution was obtained from eggshell

https://doi.org/10.1021/acsomega.3c07135
ACS Omega 2024, 9, 955−969

powders, as described in our recent publication.[22] The calcium nitrate molar concentration was adjusted, and the pH was altered to about neutral by adding 0.1 molar sodium hydroxide solution. The same molar concentration of the sodium carbonate solution was also prepared accordingly. An equal volume of calcium nitrate and sodium carbonate solution was rapidly added and mixed within the silver colloid/polyelectrolyte suspension with stirring for 30 s at ambient temperature. The resulting suspension was centrifuged at 5000 rpm for 5 min to remove the polyelectrolyte solution and unreacted AgNPs. The obtained microspheres were washed, centrifuged 3 times, and dried in a vacuum oven at 40 °C for 24 h. The resulting vaterite calcium carbonate-AgNPs were designated as $CaCO_3$−Ag-CMC when CMC was used as the capping agent and reducing agent and as $CaCO_3$−Ag-PSS when PSS was used. The AgNP loading efficiency (LE) and vaterite $CaCO_3$ loading capacity (LC) were calculated using the following equations

$$\text{LE}\ (\%) = \frac{m_P}{m_T} \times 100 \tag{1}$$

$$\text{LC}\ (\%) = \frac{m_P}{m_V} \times 100 \tag{2}$$

Here, m_P or practical mass represents the mass of silver (mg/g) loaded in $CaCO_3$−Ag-CMC or $CaCO_3$−Ag-PSS (determined by digesting the microspheres in nitric acid and tested using -nductively coupled plasma−optical emission spectrometry (ICP−OES)), m_T is the theoretical mass of silver (mg/g) loaded in $CaCO_3$−Ag-CMC or $CaCO_3$−Ag-PSS, and m_V is the mass of vaterite $CaCO_3$.

Furthermore, the yield was calculated by dividing the practical mass of $CaCO_3$−Ag-CMC or $CaCO_3$−Ag-PSS microspheres produced for each batch by the theoretical mass of $CaCO_3$−Ag-CMC or $CaCO_3$−Ag-PSS.

2.3. Preparation of Vaterite $CaCO_3$−Ag Microsphere-Embedded PVA Film. Antimicrobial absorbent PVA films were prepared by using the solvent casting method. Briefly, PVA powders (5 wt %/v) were dissolved in distilled water at 75 °C under vigorous stirring for 6 h. Afterward, the solution was degassed using an ultrasonic bath for 5 min. The 7.5% w/w $CaCO_3$−Ag-CMC or $CaCO_3$−Ag-PSS microspheres (with respect to PVA wt %) were dispersed in 1 mL of distilled water using a magnetic stirrer for 30 min. Afterward, the 1 mL suspension was added to the PVA solution under mild stirring for another 1 h. The suspension was poured into a glass Petri dish, and film drying was carried out in a hot air oven at 40 °C for 48 h. The films obtained were denoted as PVA/$CaCO_3$−Ag-CMC and PVA/$CaCO_3$−Ag-PSS, representing the embedding of $CaCO_3$−Ag-CMC and $CaCO_3$−Ag-PSS in PVA, respectively.

2.4. Characterization. *2.4.1. Scanning Electron Microscopy (SEM) and Energy-Dispersive X-ray Spectroscopy (EDS).* The morphology and size of vaterite $CaCO_3$−Ag microspheres were observed through a field emission scanning electron microscope (FE-SEM) (JEOL JSM 7800F Tokyo, Japan) coupled with energy-dispersive X-ray spectroscopy (EDX). The samples were coated with gold before SEM measurements. The statistical image processing was performed in three stages: (1) the microsphere dimensions were measured through Digi Mizer software (Media Cybernetics, Rockville, MD), (2) size distribution (PSD) determination using software Minitab 17.2.0 (Minitab Ltd., Coventry, U.K.) to obtain the mean diameter (D_m) and their respective histograms, and (3) the elemental composition of the vaterite $CaCO_3$−Ag microspheres by ESX in the mapping mode.

2.4.2. X-ray Diffraction (XRD). The structural phase study of the vaterite $CaCO_3$−Ag microspheres was carried out by a powder X-ray diffraction (XRD) analyzer in the 2θ range of 5−80° using XRD (Model: Bruker D8 ADVANCE, MA) at a voltage of 40 kV, a current of 40 mA, and a Cu Kα (1.5606 Å) radiation source. The molar percentages of vaterite and calcite polymorphs were determined using the equations derived from the research conducted by Kontoyannis et al.[42]

$$\frac{I_C^{104}}{I_V^{110}} = 7.691 \times \frac{X_C}{X_V} \tag{3}$$

where 7.691 is the proportionality constant of the calcite and vaterite polymorph mixture, $I_C{}^{104}$ represents the intensity of the calcite diffraction plane (104), while $I_V{}^{110}$ represents the intensity of the vaterite diffraction plane (110). X_C represents the molar fraction of calcite, and X_V represents the molar fraction of vaterite ($X_C + X_V = 1$).

2.4.3. Attenuated Total Reflection (ATR) Spectroscopy. The ATR spectra of vaterite $CaCO_3$−Ag microspheres were recorded from a Bruker Tensor 27 spectrophotometer at ambient temperature. The samples were scanned over wavenumbers ranging from 4000 to 650 cm^{-1} with a resolution of 4 cm^{-1}. All of the spectra were collected after an average of 16 scans for each specimen. The active side of the films was subjected to analysis.

2.4.4. X-ray Photoelectron Spectroscopy (XPS). The oxidation state of samples was analyzed using X-ray photoelectron spectroscopy (XPS), a PHI5000 VersaProbe II (ULVAC-PHI, Japan) at the SUT-NANOTEC-SLRI Joint Research Facility, Synchrotron Light Research Institute (SLRI), Thailand. A monochromatized Al−Kα X-ray source ($h\gamma$ = 1486.6 eV) was utilized to excite the samples. The XPS spectra were fitted by using PHI MultiPak XPS software with a combination of Gaussian−Lorentzian lines. Shirley-type background was used to remove the background from the spectrum before the peak fitting. The survey spectra were recorded with an energy step of 1.000 eV and a pass energy of 117.4 eV; meanwhile, the high-resolution spectra were recorded with an energy step of 0.05 eV and a pass energy of 46.95 eV. The C 1s spectrum was used as the peak reference by marking the C−C/C−H at 284.8 eV.

2.4.5. Thermogravimetric Analysis (TGA) and Differential Scanning Calorimetry (DSC). The thermal analysis was carried out using a TGA/DSC analyzer (STARe System Mettler Toledo, Columbus, OH). The samples (5 mg) were heated from 30 to 700 °C at a heating rate of 10 °C min^{-1} under a nitrogen flow with the rate of 20 mL min^{-1}. The degree of crystallinity (X_c) was calculated from the following formula[43]

$$X_c = \frac{\Delta H_m}{\Delta H_m^0} \frac{1}{X_p} \tag{4}$$

where ΔH_m is the heat of melting of the PVA polymer, $\Delta H_m{}^0$ is the heat required for melting of the 100% crystalline PVA polymer (138.60 J g^{-1}),[44] and X_p is the PVA polymer weight fraction.

2.4.6. Nanoindentation. The nanomechanical measurements were carried out with a NanoTest indenter (Micro Materials, Wrexham, U.K.) platform 3 with a Berkovich triangular diamond pyramid indenter followed by ASTM E2546−07. A loading rate of 60 mN was held for 10 s before

https://doi.org/10.1021/acsomega.3c07135
ACS Omega 2024, 9, 955−969

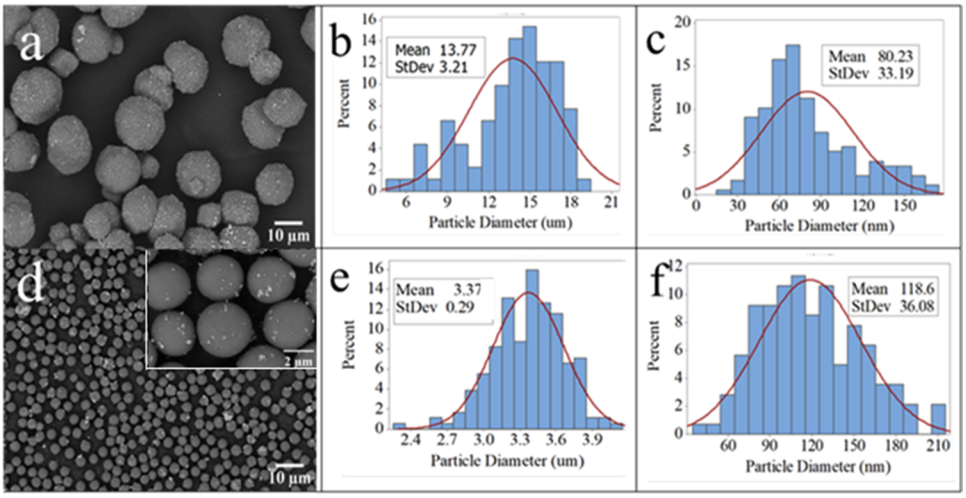

Figure 1. (a) SEM image of vaterite $CaCO_3$−Ag in the presence of CMC, (b) microsphere size distribution of vaterite $CaCO_3$−Ag in the presence of CMC, (c) AgNP size distribution of vaterite $CaCO_3$−Ag in the presence of CMC, (d) SEM image of vaterite $CaCO_3$−Ag in the presence of PSS (inset, higher magnification), (e) microsphere size distribution of vaterite $CaCO_3$−Ag in the presence of PSS, and (f) AgNP size distribution of vaterite $CaCO_3$−Ag in the presence of PSS.

the indenter was unloaded. Ten different indents were performed on each sample in randomly selected locations to obtain average hardness and reduced modulus values.

2.4.7. Cell Cytotoxicity Assay. The 3-(4,5-dimethylthiazol-2-yl)-2,5-diphenyltetrazolium bromide (MTT) tetrazolium reduction cell survival assay was used to determine the effect of the PVA polymer before and after embedding with $CaCO_3$−Ag on human dermal fibroblast (HDF) cell viability. The HDF cells were purchased from American Type Culture Collection (ATCC). Briefly, HDF cells were seeded on 96-well plates at a 7×10^4 cells/well density. The samples were disinfected by UV light sterilization for 15 min. The culture medium (DMEM, 4.5 g/L glucose, SA) supplemented with 1% penicillin/streptomycin was added to the samples and incubated overnight at 25 °C. Cells were then treated with prepared samples in a 50 mg/mL concentration for 24 h. Then, MTT solution was added to each well and incubated at 37 °C in the dark for 4 h, the formazan crystal was dissolved with DMSO, and the absorbance of the formazan solution was read at 570 nm by using a microplate reader (BMG Labtech, Ortenberg, Germany). The 50% inhibitory concentration (IC_{50}) was obtained from the dose−response curve of percent viability (Y) versus the concentration tested (X) and calculated with a linear regression performed using Microsoft Excel. All experiments were performed in triplicates, and data were expressed as mean ± standard deviation. Statistical analysis was performed using Student's t test (SPSS version 26.0, SPSS Inc.) to compare means from two independent sample groups. $^*p < 0.05$, $^{**}p < 0.01$, and $^{***}p < 0.001$ were considered statistically significant.

2.4.8. Disk-Diffusion Susceptibility Test. Antimicrobial activities were investigated by the agar disc diffusion assay followed by the procedure detailed by Weng et al.[45] with some modifications. Melted sterilized plate count agar (90 mL) was solidified in a Petri dish. *E. coli* (TISTR 527 was obtained from Thailand Institute of Scientific and Technological Research) cultured was spread on the agar surface using a sterile cotton-tipped swap under aseptic conditions. Sterile discs were placed on the spread plate, and then 10 μL of samples (10 mg/mL) or film samples (6 mm in diameter) was added to the discs. After incubation at 37 °C for 24 h, the growth inhibition zone was measured with a ruler on a millimeter scale, including discs. Each sample was made in duplicate. A single colony of *E. coli* was inoculated into 5 mL of tryptone soya broth and incubated at 37 °C for 24 h to obtain 10^6−10^7 CFU before antimicrobial testing. Whatman filter was punched to make discs (6 mm in diameter) and sterilized by an autoclave for 15 min at 121 °C to obtain sterile discs.

2.4.9. Release Studies of AgNPs from the $CaCO_3$−Ag/PVA. The release of AgNPs from $CaCO_3$−Ag-CMC, $CaCO_3$−Ag-PSS, PVA/$CaCO_3$−Ag-CMC, and PVA/$CaCO_3$ Ag-PSS films was conducted based on the techniques reported by Ferreira et al.[46] with slight modifications. The release of AgNPs in both closed-like and open-like systems was investigated under slightly acidic pH (pH 6, acetate buffer). In the closed-like conditions, the samples were incubated in the corresponding buffer solutions at 37 °C with a concentration of 2 mg/mL. At various time intervals (1, 6, 12, 24, and 48 h), an aliquot equal to 5% of the volume was collected for silver quantification using ICP-OES. The collected aliquots were then replaced with an equal volume of fresh buffer to maintain the same final volume. In the open-like conditions, both films and powders were incubated in the respective buffer at 37 °C with a concentration of 2 mg/mL. Like the closed-like conditions, at various time intervals (1, 6, 12, 24, and 48 h), an aliquot equal to 75% of the total volume was collected for silver quantification using ICP-OES. The collected aliquots were replaced with an equivalent amount of fresh buffer to maintain the final volume. All experiments were carried out in triplicate.

2.4.10. Water Absorption-Erosion. The films' water absorption and erosion properties were measured in an aqueous salt solution of phosphate buffer (PBS) at a pH of 7.4. The films with a specific size (1.5 cm × 1.5 cm) were weighed (W_1) and immersed in the PBS for 24 h. The films were withdrawn from the solution, washed several times with water, weighed, and recorded as W_2 (the surface of all of the films was dried with tissue paper before recording the W_2). Finally, the films were dried in a hot air oven for 8 h at 60 °C, and their weight was recorded as W_3. The percentages of water sorption and erosion of the films were calculated according to the following equations

https://doi.org/10.1021/acsomega.3c07135
ACS Omega 2024, 9, 955−969

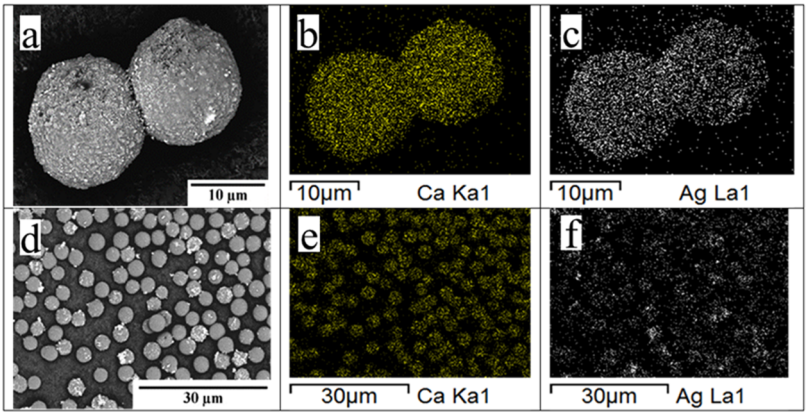

Figure 2. (a) SEM image of vaterite $CaCO_3$−Ag microspheres in the presence of CMC, (b) Ca EDS image mapping, (c) silver EDS mapping image, (d) SEM image of vaterite $CaCO_3$−Ag microspheres in the presence of PSS, (e) Ca EDS mapping image, and (f) silver mapping image.

Table 1. Yield, Size, Loading Efficiency (LE), Loading Capacity (LC), and Mass of AgNPs (mg/g) of $CaCO_3$−CMC and $CaCO_3$−Ag-PSS Microspheres

sample	yield (%)	LE (%)	LC (%)	Ag (mg/g)	size of microspheres (μm)
$CaCO_3$−Ag-CMC	91.29 ± 3.57	22.94 ± 0.53	1.4 ± 0.03	13.77 ± 0.32	13.77 ± 3.21
$CaCO_3$−Ag-PSS	82.51 ± 8.51	31.71 ± 1.51	1.94 ± 0.09	19.02 ± 0.91	3.37 ± 0.29

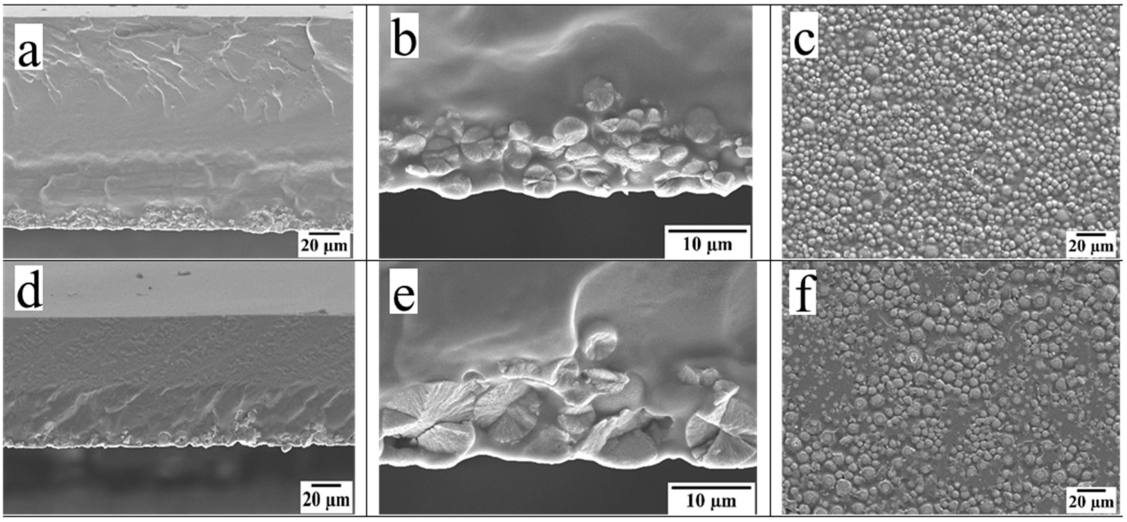

Figure 3. (a) Cross-sectional SEM image of PVA/$CaCO_3$−Ag-PSS, (b) higher magnification of image (a), (c) SEM surface image of PVA/$CaCO_3$−Ag-PSS, (d) cross-section SEM image of PVA/$CaCO_3$−Ag-CMC, (e) higher magnification of image (d), and (f) SEM surface image of PVA/$CaCO_3$−Ag-CMC.

$$\text{water absorption (\%)} = \left[\frac{(W_2 - W_3)}{W_3}\right] \times 100 \quad (5)$$

$$\text{water erosion (\%)} = \left[\frac{(W_1 - W_3)}{W_1}\right] \times 100 \quad (6)$$

3. RESULTS AND DISCUSSION

3.1. Morphological Study. SEM analysis was performed to observe the morphological characteristics of the precipitated vaterite $CaCO_3$−Ag with two different reducing agents and stabilizers (i.e., CMC and PSS). As illustrated in Figure 1a, by precipitation in the Ag-CMC colloid, larger spherical-shaped $CaCO_3$ microspheres and smaller AgNPs were observed compared to precipitation of calcium carbonate in the Ag-PSS colloid (Figure 2b). Using PSS as a reducing agent and stabilizer narrowed the particle size distribution (PSD) and their mean diameter (D_m) in comparison with using CMC. The particle diameters of $CaCO_3$ and AgNPs vs their percentages are plotted as histograms and shown in Figure 1. The histogram of $CaCO_3$−Ag-CMC in Figure 1b shows that the maximum size distribution is in the range of 12−18 μm with a D_m of 13.2 μm. The range significantly decreased to 3−3.6 um with a D_m of 3.3 μm with switching of the reducing agent and stabilizer to PSS in $CaCO_3$−Ag-PSS, as shown in Figure 1e. Additionally, Table 1 illustrates that a higher AgNP loading efficiency (LE) and vaterite $CaCO_3$ loading capacity (LC) were achieved in $CaCO_3$−Ag-PSS in comparison to $CaCO_3$−Ag-CMC, attributed to the smaller particle size and higher surface-area-to-volume ratio. However, the yield was lower, possibly because of some loss during the product washing process due to their smaller sizes. However,

https://doi.org/10.1021/acsomega.3c07135
ACS Omega 2024, 9, 955−969

higher values for PSD and D_m were observed for AgNPs in $CaCO_3$−Ag-PSS (i.e., PSD of 60−180 nm, D_m of 118.6 nm) compared to $CaCO_3$−Ag-CMC (PSD of 40−120 nm, D_m of 80 nm). Figure 2 shows the energy-dispersive X-ray spectroscopy (EDS) mapping images of the vaterite $CaCO_3$ microspheres loaded with AgNPs precipitating in silver colloids reduced by PSS and CMC polyelectrolytes. The AgNPs loaded homogeneously on vaterite $CaCO_3$ microspheres (Figure 2d) in the CMC polyelectrolyte. However, as shown in Figure 2f, AgNPs showed slight agglomeration at some vaterite $CaCO_3$ microspheres. Furthermore, EDS weight percentage (wt %) elemental analysis revealed that the average wt % of silver atom loaded in vaterite $CaCO_3$ microspheres in the presence of CMC was higher (16.64 ± 0.92 wt %) than in the vaterite $CaCO_3$ microspheres in the presence of PSS (14.37 ± 2.30 wt %).

Cryogenic cross-section and surface SEM analyses were performed to observe the morphological characteristics of the PVA film after embedding with vaterite $CaCO_3$−Ag microspheres. As illustrated in Figure 3 for PVA/$CaCO_3$−Ag-PSS and PVA/$CaCO_3$−Ag-CMC, the cross-sectional image shows a bilayer structure film possessing active and inactive layers with a total thickness of 96.4 ± 30.1 μm. The active layer with a thickness of 12.6 ± 2.8 μm contains vaterite $CaCO_3$−Ag microspheres, and the inactive layer with a thickness of 90.2 ± 32.8 μm consists of only the PVA polymer matrix. The bilayer formation occurred from the sedimentation of vaterite $CaCO_3$−Ag microspheres in the PVA polymer matrix, arising due to their large contact surface area and high correlation energy during the drying process.[47] The advantage of the bilayer structure is that the inactive layer would serve as an extra structural supporting and water absorbency layer for the active layer, while the active layer interacts with the environment containing microorganisms.

Furthermore, the surface analysis (Figure 3c) revealed the distribution of vaterite $CaCO_3$−Ag-PSS microspheres across the active layer in the PVA matrix. However, $CaCO_3$−Ag-CMC is less distributive in the PVA matrix due to the size of microspheres or differences in the interactions between the CMC and the PVA matrix. Figure 4 shows the cross-sectional and surface EDS mapping images of the PVA/$CaCO_3$−Ag-CMC and PVA/$CaCO_3$−PSS films. The EDS elemental analysis revealed that the average weight percentage (wt %) of silver atoms on the surface of PVA/$CaCO_3$−Ag-CMC was 1.04 ± 0.05 wt %, while in the cross section, it was 0.80 ± 0.315 wt %. In contrast, in PVA/$CaCO_3$−Ag-PSS, the average wt % of silver atoms in the cross-sectional analysis was notably lower at 0.71 ± 0.20 wt % compared to the surface analysis, where it measured 1.02 ± 0.005 wt %. The observed discrepancy could be attributed to a nonequivalence effect, which might be influenced by various factors including matrix effects, heterogeneous distribution of particles, and other potential interactions between the sample and the analytical technique.

3.2. Structural Study. The XRD fingerprints of the PVA polymer film, $CaCO_3$−Ag-CMC, $CaCO_3$−Ag-PSS, PVA/$CaCO_3$−Ag-PSS, and PVA/$CaCO_3$−Ag-CMC films are shown in Figure 5A. The XRD pattern of the neat PVA polymer film, as illustrated in Figure 5A,a, shows a sharp peak at 2θ = 20° corresponding to the crystalline domain of PVA chains.[48] According to the XRD results shown in Figure 5A,b, the fingerprint of vaterite $CaCO_3$−Ag precipitated in the presence of silver colloid and CMC shows distinct peaks at 2θ values of 19.5, 21, 25, 27.2, 29.5, 32.8, 34.1, 43.9, 49, 50.1, and 55.8°, confirming the dominant vaterite polymorph over the calcite

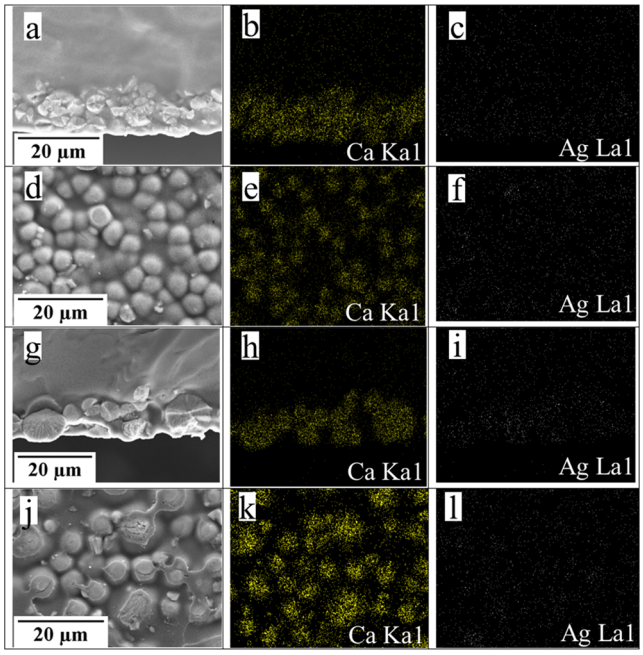

Figure 4. (a) Cross-section SEM image of vaterite $CaCO_3$−Ag microspheres in the presence of PSS, (b) Ca EDS image mapping, (c) silver EDS mapping image, (d) active surface SEM image of vaterite $CaCO_3$−Ag microspheres in the presence of PSS, (e) Ca EDS mapping image, and (f) silver mapping image, (g) cross-section SEM image of PCC microspheres in the presence of CMC, (h) Ca EDS image mapping, (i) silver EDS mapping image, (j) active surface SEM image of vaterite $CaCO_3$−Ag microspheres in the presence of CMC, (k) Ca EDS mapping image, and (l) silver mapping image.

polymorphs. However, as shown in Figure 5A,c, using PSS as a reducing agent and stabilizer, the characteristic calcite XRD peak at 2θ of 29.5° disappears, indicating the sole formation of a vaterite polymorph crystal structure and the absence of calcite polymorphs. It is worth mentioning that the shoulder peak at 2θ of 34.1° indicates the vaterite polymorphs loaded with AgNPs. As shown in Figure 5A,d,e, after embedding the vaterite $CaCO_3$−Ag in the PVA polymer matrix, the shoulder peak at 2θ of 34.1° disappeared due to the coating properties of the PVA polymer matrix covering the microspheres. Furthermore, as shown in Figure 5A,e, the intensity of the characteristic calcite peak at 2θ of 29.1° increased slightly, indicating the semi-conversion of vaterite to a calcite polymorph structure after embedding into the PVA polymer matrix. However, the vaterite polymorph is still the only structure, as shown in Figure 5A,d, without a calcite peak. Furthermore, the calcite and vaterite mole percentages were calculated based on the reflection peaks at 104 (2θ of 29.5°) for calcite and 110 (2θ of 29.5°) for vaterite as suggested by Kontoyannis et al.[42] The findings indicate that $CaCO_3$−Ag-CMC has a vaterite polymorph composition of 90.7 mol %. However, after being embedded in a PVA polymer matrix, the vaterite content slightly decreases to 86.1 mol %, suggesting a minor shift toward the calcite polymorph. On the other hand, the data reveals that the polymorph composition of $CaCO_3$−Ag-PSS remains entirely vaterite even after embedding in the PVA polymer matrix.

Figure 5B also shows the infrared spectra of the PVA film, $CaCO_3$−Ag-CMC, $CaCO_3$−Ag-PSS, PVA/$CaCO_3$−Ag-PSS, and PVA/$CaCO_3$−Ag-CMC. The spectrum of the neat PVA shows a broadband at 3268 cm^{-1} due to the hydroxyl functional groups. The bands at 2910 and 2942 cm^{-1} are due to the

https://doi.org/10.1021/acsomega.3c07135
ACS Omega 2024, 9, 955−969

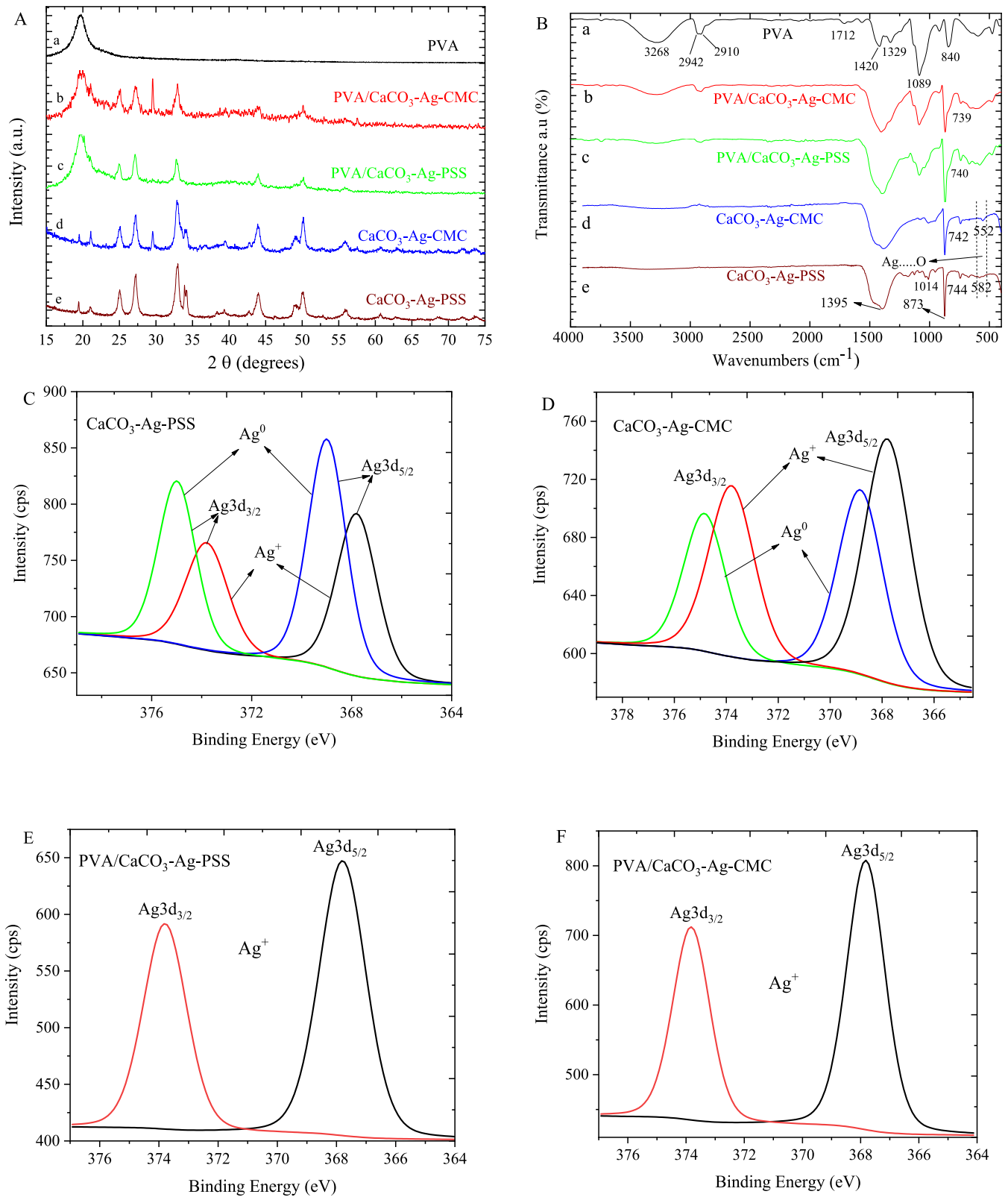

Figure 5. (A) XRD fingerprints and (B) ATR spectra of (a) PVA, (b) PVA/$CaCO_3$−Ag-CMC, (c) PVA/$CaCO_3$−Ag-PSS, (d) $CaCO_3$−Ag-CMC, and (e) $CaCO_3$−Ag-PSS. Ag 3d XPS deconvolution scans of (C) $CaCO_3$−Ag-PSS, (D) $CaCO_3$−Ag-CMC, (E) PVA/$CaCO_3$−Ag-PSS, and (F) PVA/$CaCO_3$−Ag-CMC.

stretching vibrations of CH and CH_2 groups and the bands at 1329 and 1420 cm^{-1} are attributed to their deformation vibration. The band at 1712 cm^{-1} is the characteristic peak of the carbonyl group from the acetate groups of poly(vinyl acetate).[49] Furthermore, the bands at 1089 and 840 cm^{-1} are attributed to C−O and C−C stretching vibrations, respectively. The spectra of $CaCO_3$−Ag-CMC and $CaCO_3$−Ag-PSS show four vibrational modes of carbonate ions at 1395 cm^{-1} assigned to

https://doi.org/10.1021/acsomega.3c07135
ACS Omega 2024, 9, 955−969

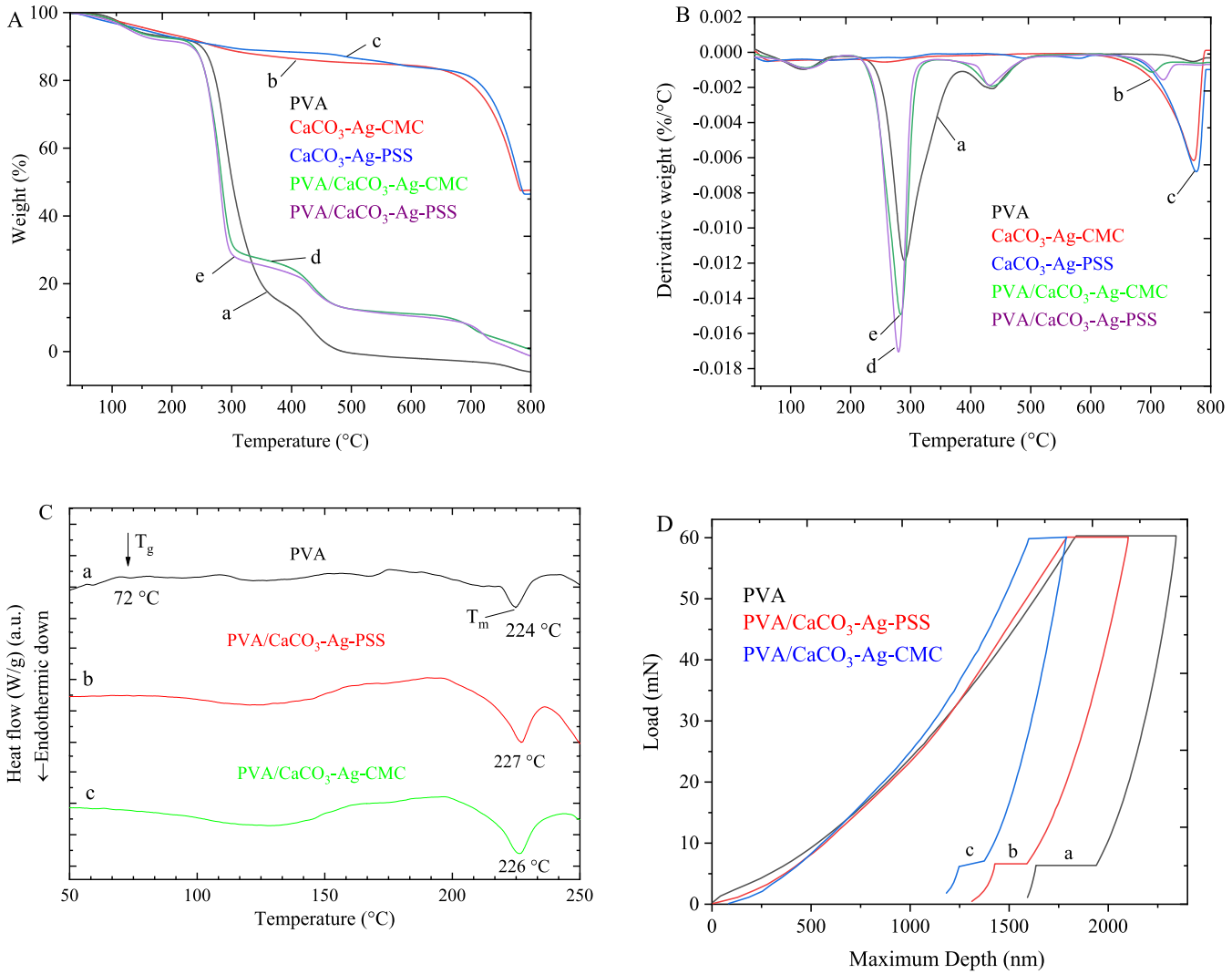

Figure 6. (A) TGA and (B) DTG plots of (a) PVA, (b) $CaCO_3$−Ag-CMC, (c) $CaCO_3$−Ag-PSS, (d) PVA/$CaCO_3$−Ag-CMC, and (e) PVA/$CaCO_3$−Ag-PSS. (C) DSC thermograms of (a) PVA, (b) PVA/$CaCO_3$−Ag-PSS, and (c) PVA/$CaCO_3$−Ag-CMC. (D) Load−displacement curves for (a) PVA, (b) PVA/$CaCO_3$−Ag-PSS, and (c) PVA/$CaCO_3$−Ag-CMC.

asymmetric stretching, at 1014 cm^{-1} attributed to symmetric stretching, at 872 cm^{-1} assigned to out-of-plane bending, and at 713 cm^{-1} ascribed to in-plane bending vibrations and one vibrational mode of AgNPs at 552−582 cm^{-1}.[22] $CaCO_3$−Ag-PSS and $CaCO_3$−Ag-CMC microspheres (7.5 wt %) in the PVA polymer matrix lead to the shift of some peaks and change of relative intensities. The intensity of the hydroxyl peaks at 3268 cm^{-1} and the carbonyl group at 1712 cm^{-1} decreased significantly, indicating the intermolecular interaction between PVA macromolecular chains and calcium carbonate microspheres. Hence, we can conclude that the integration of vaterite $CaCO_3$−Ag microspheres into the PVA polymer matrix is not solely characterized by physical entrapment. Instead, this integration leads to a uniform distribution of particles throughout the matrix.

To identify the valence state of AgNPs, a deconvolution X-ray photoelectron spectroscopy (XPS) scan was conducted on Ag 3d for vaterite $CaCO_3$−Ag before and after embedding in the PVA polymer matrix. The deconvolution XPS scan for silver ion (Ag^+) and metallic silver (Ag^0) reveals two spin−orbit splittings of Ag $3d_{5/2}$ and Ag $3d_{3/2}$ peaks (Figure 5C,D) with binding energies (B.Es) of 367.80, 373.80 and 368.84, 374.84 eV for $CaCO_3$−Ag-CMC and B.Es of 367.80, 373.80 and 368.99, 374.99 eV for $CaCO_3$−Ag-PSS, respectively. These B.E values indicated the presence of Ag^+ and Ag^0 valence states before embedding into the PVA polymer matrix.[50,51] The lower B.E values suggested the presence of Ag^+ in addition to Ag^0.[52,53] However, as shown in Figure 5E,F, after embedding the vaterite $CaCO_3$−Ag in the PVA polymer matrix, only one spin−orbit splitting of Ag $3d_{5/2}$ and Ag $3d_{3/2}$ peaks with B.Es of 367.80, 373.80 and of 367.82, 373.82 eV was observed for PVA/$CaCO_3$−Ag-PSS and PVA/$CaCO_3$−Ag-CMC, respectively. The sole presence of Ag^+ is presumably due to the surface oxidation of the AgNPs and their release during the embedding in the PVA polymer matrix.[54] Ag^+ ions are highly reactive and can exert their antimicrobial effects at very low concentrations. Their small size allows them to penetrate into microbial cells and interfere with various cellular processes, leading to inhibition of microbial growth and ultimately causing microbial death.[55]

3.3. Thermal Behaviors. The thermal behavior of the PVA, vaterite $CaCO_3$−Ag, and their resulting films was characterized using thermogravimetric-differential thermal analysis (TG-DTG) methods. Even though wound dressings are used at body temperature, understanding the behavior of PVA/

https://doi.org/10.1021/acsomega.3c07135
ACS Omega 2024, 9, 955−969

$CaCO_3$−Ag films across a broader temperature range can offer insights into their overall thermal stability and potential applications. For instance, wound dressing films often undergo sterilization processes, which can involve exposure to elevated temperatures, or in some cases, they may be subjected to hyperthermal therapies, where localized heating is applied to promote healing. As illustrated in Figure 6A,B, the neat PVA film underwent two major weight loss stages, i.e., major degradation onset at 253 °C and endset at 356 °C (76.5 wt loss %) and second degradation onset at 396 °C and endset at 492 °C (13.5 wt lost %).[56] The former was due to the decomposition of PVA backbone chains, and the latter resulted from volatile saturated and unsaturated aldehydes and ketones produced from the major stage of degradation.[57] Both $CaCO_3$−Ag-PSS and $CaCO_3$−Ag-CMC underwent one step of thermal degradation at onset temperatures of 700 and 687 °C to the endset temperatures of 789 and 787 °C with equal wt loss % values of 36.4 and 36.5, respectively. The weight loss was due to the decomposition of carbonate functional groups and, consequently, the conversion of calcium carbonate to calcium oxide.[58] Therefore, the incorporation of vaterite $CaCO_3$−Ag in the PVA film resulted in three main stages of degradation. The major stage (64.5%), second stage (13.7%), and third stage (6.5%) of weight losses for PVA/$CaCO_3$−Ag-PSS were observed over the onset and endset temperatures at 235 to 306, 399 to 483, and 655 to 720 °C, respectively. In PVA/$CaCO_3$−Ag-CMC, the major stage (64%) and second stage (10.1%) of degradation occurred at onset temperatures of 239 and 303 and 411 and 481 °C, respectively. The final stage (7.1%) of degradation appeared at the narrower temperature range of onset 691 °C and endset 736 °C in comparison to PVA/$CaCO_3$−Ag-PSS. This could indicate the better compatibility of $CaCO_3$−Ag-CMC with the PVA polymer matrix than $CaCO_3$−Ag-PSS. The maximum degradation temperature (T_{max}) of the neat PVA polymer film was 289.7 °C, which slightly decreased upon embedding of vaterite $CaCO_3$−Ag to 282.5 °C (for PVA/$CaCO_3$−Ag-PSS) and to 279.7 °C (for PVA/$CaCO_3$−Ag-CMC) (Table 2).

Table 2. Thermal Property Parameters

sample name	T_g (°C)	T_m (°C)	ΔH (J/g)	crystallinity (X_c,%)	T_{max} (°C)
PVA	72	224	11.9	8.6	289.7
$CaCO_3$−Ag-CMC	n/a	n/a	n/a	n/a	777
$CaCO_3$−Ag-PSS	n/a	n/a	n/a	n/a	774
PVA/$CaCO_3$−Ag-CMC	n/a	226	27.1	21.2	279.7
PVA/$CaCO_3$−Ag-PSS	n/a	227	29.7	23.1	282.5

The DSC thermograms of PVA and its resulting vaterite $CaCO_3$−Ag-embedded films are shown in Figure 6C. The DSC curve for the neat PVA polymer revealed the presence of a glass-transition temperature (T_g) and melting temperature (T_m) at 79 and 224 °C, respectively, due to its semicrystalline nature. However, the DSC analysis of PVA/$CaCO_3$−Ag-PSS and PVA/$CaCO_3$−Ag-CMC films revealed the absence of T_g and a shift of T_m to higher temperatures. A disappearance of T_g and change of T_m after loading of vaterite $CaCO_3$−Ag are due to the fully crystalline nature of calcium carbonate and consequently the change of amorphous−crystalline phases in the PVA polymer matrix. The degree of crystallinity (X_c) of PVA and its composition with loaded vaterite $CaCO_3$−Ag were calculated and are summarized in Table 2. The X_c of the PVA polymer matrix was enhanced and increased to 23.1 and 21.2% in PVA/$CaCO_3$−Ag-PSS and PVA/$CaCO_3$−Ag-CMC, respectively. Higher crystalline polymer films are known for their enhanced gas barrier properties, attributed to the dense molecular arrangement characteristic of crystalline polymorphs, which reduces the permeability of gas molecules. Furthermore, heightened crystallinity not only reinforces the mechanical strength of the PVA wound dressing film but also contributes to its structural integrity.[59]

3.4. Nanomechanical Properties. To investigate the nanomechanical properties, nanoindentation tests were conducted on the neat PVA film and its compositions with $CaCO_3$−Ag-PSS and $CaCO_3$−Ag-CMC. The reduced modulus (E_r) and hardness (H) of the prepared films were determined from the load−displacement curves, presented in Figure 6D. The embedding of both $CaCO_3$−Ag-PSS and $CaCO_3$−Ag-CMC in PVA displaced the curves to lower penetration depths, which indicated higher resistance to the penetration and therefore improved deformability resistance of the PVA film against an indenter. The penetration depth becomes minimal by embedding $CaCO_3$−Ag-CMC in the PVA polymer matrix; thus, the PVA/$CaCO_3$−Ag-CMC film showed the highest hardness. The average values of reduced modulus and hardness were calculated for the neat PVA polymer matrix, and PVA embedded with $CaCO_3$−Ag-CMC and $CaCO_3$−Ag-PSS is shown in Table 3. The nanomechanical properties of the prepared PVA films are vital as they act reciprocally with the surrounding tissues chemically and mechanically. Therefore, the microspheres' release kinetics or antimicrobial properties may alter based on their mechanical interactions.[60] Overall, these mechanical improvements enhance the wound dressing's compatibility with human skin, offering both durability and comfort in its application.[61,62]

Table 3. Average Hardness and Reduced Modulus Values for PVA, PVA/$CaCO_3$−Ag-CMC, and PVA/$CaCO_3$−Ag-PSS

sample name	hardness (GPa)	reduced modulus (GPa)
PVA	0.17 ± 0.002	5.63 ± 0.06
PVA/$CaCO_3$−Ag-PSS	0.46 ± 0.09	11.77 ± 1.39
PVA/$CaCO_3$−Ag-CMC	0.64 ± 0.29	14.62 ± 5.23

3.5. In Vitro Biocompatibility. The cytotoxicity assay is essential for the products employed in the food industry and biomedical applications. Therefore, the toxicity of the vaterite $CaCO_3$−Ag and their resulting films with the PVA polymer matrix were analyzed using the MTT assay in the presence of a human dermal fibroblast (HDF) cell culture. The obtained results are presented in Table 4 and Figures 7 and 8.

Figure 7 highlights a significant finding, indicating that precipitated eggshell particles (PESPs) exhibit a higher level of cytocompatibility with human cells compared to that of ground eggshell particles (ESPs). The PESP was precipitated without

Table 4. Cell Viability and IC_{50} Results

sample name	IC_{50} (mg/mL)	cell viability (mg/mL)
ESP	45	nontoxic (≤1)
PESP	84	nontoxic (≤25)
$CaCO_3$−Ag-CMC	23	nontoxic (≤1)
$CaCO_3$−Ag-PSS	17	nontoxic (≤0.1)
PVA	459	nontoxic (≤50)
PVA/$CaCO_3$−Ag-CMC	84	nontoxic (≤5)
PVA/$CaCO_3$−Ag-PSS	63	nontoxic (≤5)

https://doi.org/10.1021/acsomega.3c07135
ACS Omega 2024, 9, 955−969

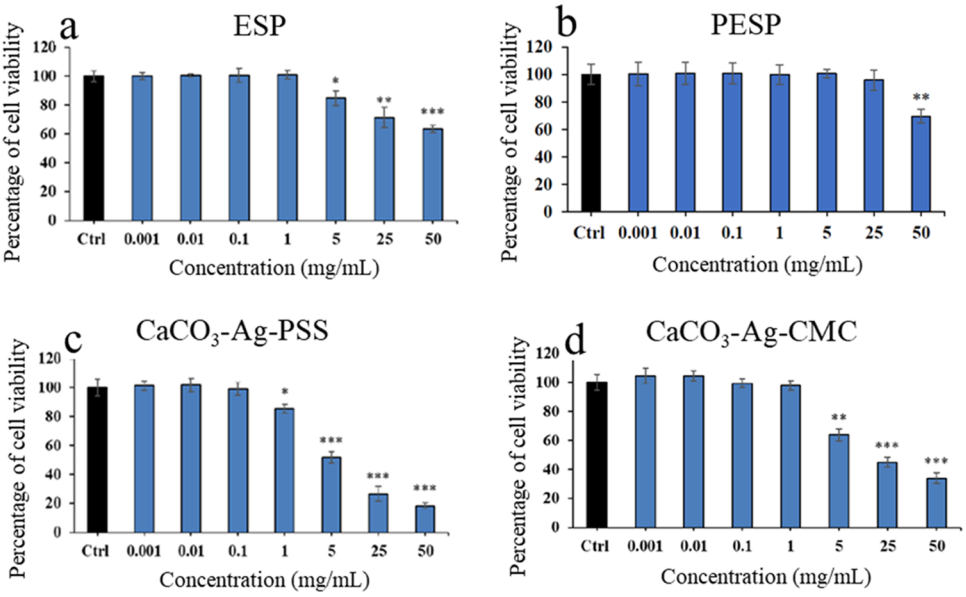

Figure 7. Cell viability (%) plot versus concentration for (a) ESP, (b) PESP, $CaCO_3$−Ag-PSS, (c) $CaCO_3$−Ag-CMC, and (d) $CaCO_3$−Ag-CMC. *p < 0.05, **p < 0.01, and ***p < 0.001 were considered statistically significant.

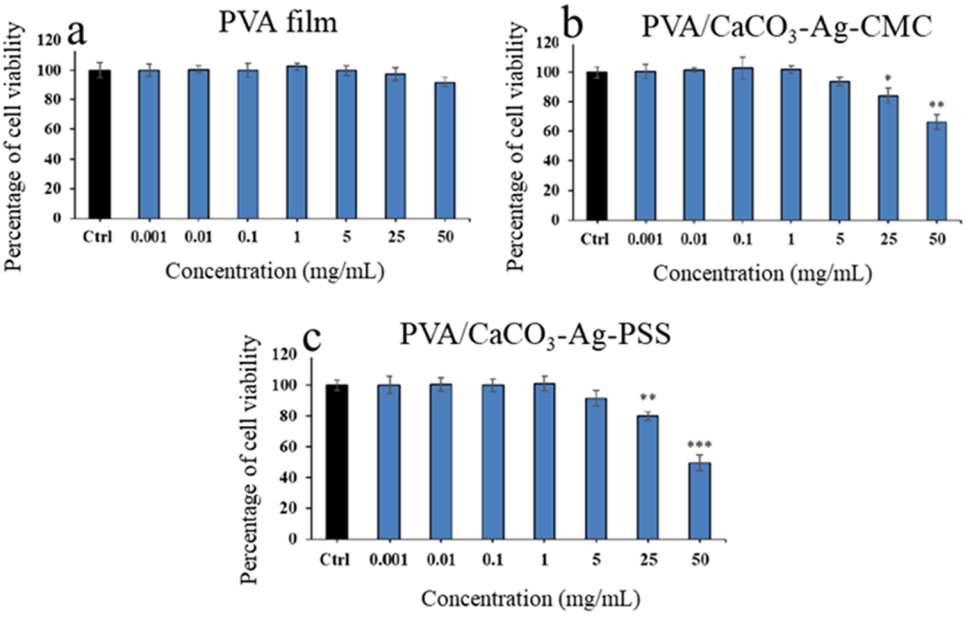

Figure 8. Cell viability (%) plot versus concentration for (a) neat PVA, (b) PVA/$CaCO_3$−Ag-CMC, and (c) PVA/$CaCO_3$−Ag-PSS. *p < 0.05, **p < 0.01, and ***p < 0.001 were considered statistically significant.

CMC and PSS. This observation underscores the efficacy of our precipitation technique in enhancing the biocompatibility of $CaCO_3$ derived from eggshells. However, we also noted that cell biocompatibility diminishes with an increase in the concentration of AgNPs in the samples. This is consistent with findings reported by Satyavani et al.,[63] who observed dose-dependent toxicity of AgNPs on the human epidermoid larynx carcinoma cell line, leading to reduced cell viability at higher AgNP concentrations.

Furthermore, we observed that $CaCO_3$−Ag-CMC and $CaCO_3$−Ag-PSS are biocompatible with no signs of toxicity at concentrations of ≤1 and 0.1 mg/mL, respectively. This information is presented in Figure 8. It is important to note that the neat PVA polymer matrix is biocompatible even at a high concentration of 50 mg/mL. However, as demonstrated in Figure 8b,c, there is a slight decrease in cell cytocompatibility when $CaCO_3$−Ag-CMC and $CaCO_3$−Ag-PSS microspheres are incorporated into the PVA matrix. Nonetheless, both PVA/$CaCO_3$−Ag-CMC and PVA/$CaCO_3$−Ag-PSS remain fully biocompatible at concentrations ≤5 mg/mL.

Additional quantitative information is provided in Table 4, where the half-maximal inhibitory concentration (IC_{50}) values are presented. IC_{50} is a crucial parameter in pharmacology and toxicology, representing the concentration of a substance required to inhibit a particular biological or biochemical process by 50%. In our study, IC_{50} values serve as a key metric for assessing the biocompatibility of the materials under investigation.

Notably, PESP, with an IC_{50} value of 84 mg/mL, exhibits approximately twice the viability with human fibroblast cells

https://doi.org/10.1021/acsomega.3c07135
ACS Omega 2024, 9, 955−969

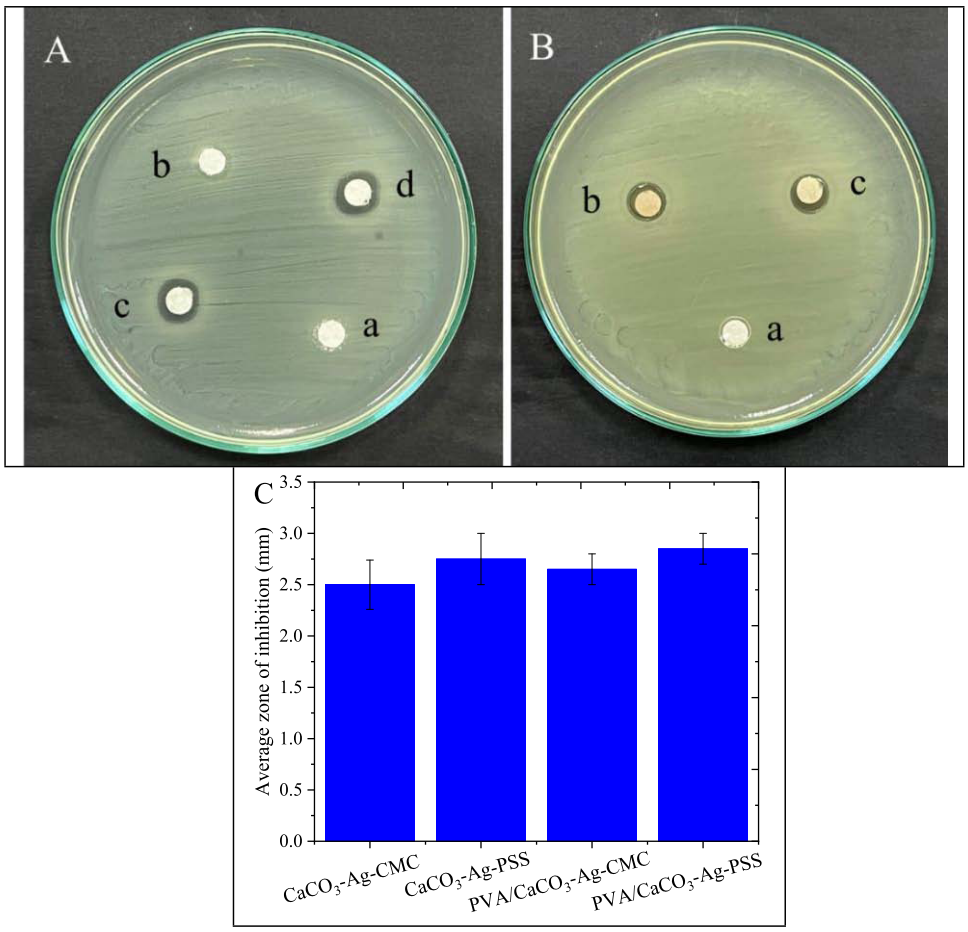

Figure 9. (A) Inhibition zones of (a) ESP (ground eggshell), (b) PESP (precipitated eggshell), (c) $CaCO_3$−Ag-CMC powder, and (d) $CaCO_3$−Ag-PSS powder. (B) Inhibition zones of (a) neat PVA, (b) PVA/$CaCO_3$−Ag-CMC, and (c) PVA/$CaCO_3$−Ag-PSS. (C) Plot of average zone of inhibition.

compared with ESP (45 mg/mL). This suggests that precipitation increases viability by purifying the $CaCO_3$ from eggshells, which may contain proteins and other compounds. Furthermore, the toxicity decreases significantly after the incorporation of $CaCO_3$−Ag-CMC and $CaCO_3$−Ag-PSS into PVA, as reflected by the increase in IC_{50} values to 84 and 63 mg/mL, respectively, from the original values of 23 and 17 mg/mL. The IC_{50} values provide valuable insights into the relative safety and compatibility of the materials with biological systems. Higher IC_{50} values signify that a substance is less toxic and can be considered more biocompatible.

3.6. Antimicrobial Activities. Antibacterial activities of ground eggshell particles (ESPs), precipitated eggshell particles (PESPs), $CaCO_3$−Ag-CMC, $CaCO_3$−Ag-PSS, neat PVA, PVA/$CaCO_3$−Ag-CMC, and PVA/$CaCO_3$−Ag-PSS were examined with *E. coli* bacterial strains. As shown in Figure 9, ESP, PESP, and PVA film have no antibacterial activity against *E. coli* bacteria. However, vaterite $CaCO_3$−Ag and its incorporation into the PVA polymer matrix showed antimicrobial activities. The zones of inhibition for $CaCO_3$−Ag-CMC and $CaCO_3$−Ag-PSS onto *E. coli* disc were 2.50 ± 0.24 and 2.75 ± 0.25 mm, respectively. The zones of inhibition slightly changed to 2.65 ± 0.15 and 2.85 ± 0.15 mm in PVA/$CaCO_3$−Ag-CMC and PVA/$CaCO_3$−Ag-PSS, respectively. PVA might improve the adhesion of the microspheres to the surface of the bacterial disc, allowing for a more efficient transfer of the AgNPs and, subsequently, an increased zone of inhibition. The obtained inhibition zones in our study are in accordance with a survey reported by Pencheva et al.,[64] higher than the reported data by Eghbalifam et al.,[65] and lower than the reported data by Tripathi et al.[66] Even though both $CaCO_3$−Ag-CMC and $CaCO_3$−Ag-PSS are different in size and distribution (as stated earlier in the morphology section), almost similar antimicrobial properties were obtained for both. This indicates that the sizes of loaded AgNPs and vaterite $CaCO_3$−Ag microspheres have not significantly affected the films' antimicrobial activities in this study.

3.7. Release Study of AgNPs. The AgNP release experimental procedures were employed to examine the release behavior of silver from the vaterite $CaCO_3$−Ag microspheres and also after their embedding in PVA polymer over time under very acetic pH conditions. The release of AgNPs from vaterite $CaCO_3$−Ag was assessed under two different conditions, closed and open conditions, in order to understand how the release of AgNPs is affected by the surrounding environment and how different factors may influence the controlled release process. In the closed condition, the vaterite $CaCO_3$−Ag microspheres were confined, simulating a restricted environment, which might mimic certain wound dressing applications. On the other hand, the open-like condition aimed to represent a more unrestricted environment, simulating scenarios where the vaterite-containing materials are exposed to the surrounding medium without confinement.

Figure 10A illustrates the release of silver ions from $CaCO_3$−Ag-CMC and $CaCO_3$−Ag-PSS. It is evident that $CaCO_3$−Ag-

https://doi.org/10.1021/acsomega.3c07135
ACS Omega 2024, 9, 955−969

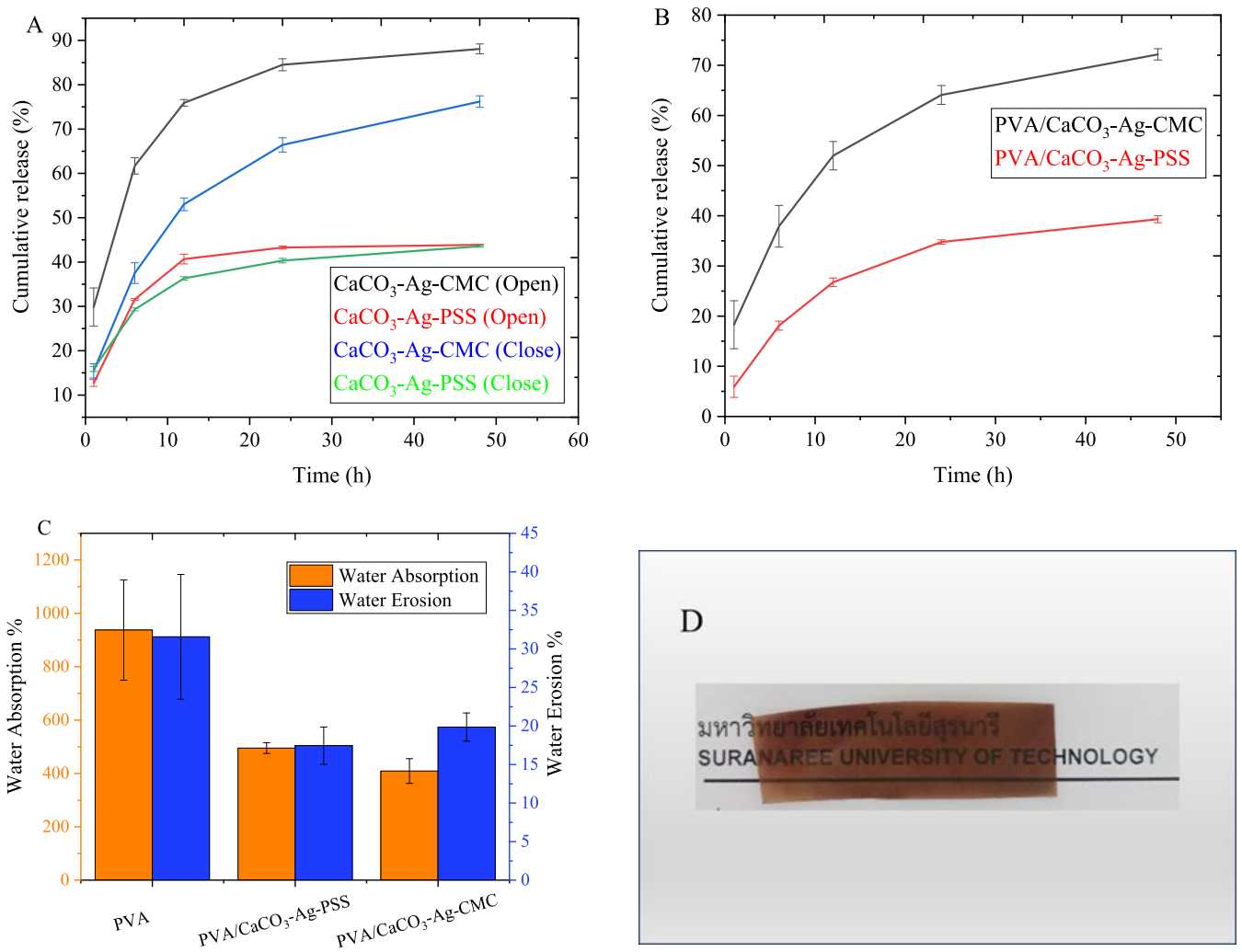

Figure 10. (A) Ag ions' cumulative release from $CaCO_3$−Ag-CMC and $CaCO_3$−Ag-PSS microspheres at pH 6 at closed and open conditions. (B) Ag ions' cumulative release of PVA/$CaCO_3$−Ag-CMC and PVA/$CaCO_3$−Ag-PSS films at pH 6 at open conditions. (C) Water absorption and erosion of PVA, PVA/$CaCO_3$−Ag-PSS, and PVA/$CaCO_3$−Ag-CMC films. (D) Optical image of the PVA/$CaCO_3$−Ag-PSS film.

CMC exhibits a higher release compared to $CaCO_3$−Ag-PSS in both closed and open conditions. Under open conditions, $CaCO_3$−Ag-CMC displayed a rapid release of 29.9% (4.1 mg/g) of Ag ions within the first hour, reaching a maximum of 88% (12.1 mg/g) in 48 h. Conversely, under closed conditions, the release was slower, with a maximum of 76.2% (10.5 mg/g) released within 48 h. For $CaCO_3$−Ag-PSS under open conditions, the initial release was 12.7% (2.41 mg/g) at the first hour, half of what was observed in $CaCO_3$−Ag-CMC. The maximum Ag release of 43.8% (8.3 mg/g) was observed after 48 h of incubation in the acetate buffer solution. The release profile was quite similar under both closed and open conditions for $CaCO_3$−Ag-PSS. These results highlight the significance of selecting the appropriate capping agent between CMC and PSS for AgNPs. This knowledge can be leveraged in designing tailored wound dressings, allowing for faster release rates in the early hours with CMC or slower release rates with PSS as desired.

The release of Ag ions from PVA/$CaCO_3$−CMC and PVA/$CaCO_3$−Ag-PSS was investigated under open conditions, as depicted in Figure 10B. The results show that 72.17% (9.9 mg/g) and 39.32% (7.5 mg/g) Ag ions were released from PVA/$CaCO_3$−Ag-CMC and PVA/$CaCO_3$−Ag-PSS, respectively, within 48 h. This indicates that the PSS capping agent delayed the release of AgNPs, and the incorporation of vaterite $CaCO_3$−Ag into the PVA matrix further contributed to the slower release, reducing the Ag-ion release by approximately 14% in $CaCO_3$−Ag-CMC and 2% in $CaCO_3$−Ag-PSS.

3.8. Water Absorption and Erosion. The level of water absorption and aqueous erosion in vaterite $CaCO_3$−Ag-embedded PVA films may customize the antimicrobial, biocompatibility, and biodegradation rates of PVA films. The water absorption and aqueous erosion percentages of the PVA films were measured and are presented in Figure 10C. The optical image of the PVA/$CaCO_3$−Ag-PSS film is shown in Figure 10D. The water absorption percentages for PVA, PVA/$CaCO_3$−Ag-PSS, and PVA/$CaCO_3$−Ag-CMC were 937 ± 188, 495 ± 20, and 409 ± 46%, respectively. The water absorption capacities of PVA/$CaCO_3$−Ag-PSS and PVA/$CaCO_3$−Ag-CMC were lower than neat PVA due to the internal bonding possibility between PVA macromolecular chains and vaterite $CaCO_3$−Ag microspheres. This is in accordance with the ATR results. It is interesting to note that PVA/$CaCO_3$−Ag-CMC has an even lower water absorption capacity than PVA/$CaCO_3$−Ag-PSS, probably due to its larger sizes of $CaCO_3$−Ag-CMC compared to $CaCO_3$−Ag-PSS. The water absorption capacity

https://doi.org/10.1021/acsomega.3c07135
ACS Omega 2024, 9, 955−969

required for wound dressing films can vary widely based on factors such as wound type, wound depth, patient condition, and the specific phase of wound healing. For instance, dry wounds may benefit from wound dressing films with lower water absorption to provide some moisture without risking over-hydration. Conversely, exuding wounds typically require wound dressings with higher water absorbency due to the substantial amount of fluid or exudate they produce.[67,68] The aqueous erosion percentages for PVA, PVA/$CaCO_3$−Ag-PSS, and PVA/$CaCO_3$−Ag-CMC were 31.6 ± 8.1, 17.5 ± 2.4, and 20 ± 1.8%, respectively. The erosion percentages in PVA/$CaCO_3$−Ag-PSS and PVA/$CaCO_3$−Ag-CMC were lower than that of the neat PVA polymer film. This might be derived from the intermolecular interaction after embedding vaterite $CaCO_3$−Ag, which reduced the PVA erosion percentages. However, PVA/$CaCO_3$−Ag-PSS and PVA/$CaCO_3$−Ag-CMC showed roughly the same aqueous erosion percentage. Water erosion can affect strength and elasticity, in which lower water erosion can lead to a stronger and more flexible film during service as a wound dressing.

4. CONCLUSIONS

This study underscores the potential of the vaterite polymorph of $CaCO_3$, as a carrier for the controlled and stable release of AgNPs. Vaterite $CaCO_3$−Ag microspheres were initially obtained using different reducing and capping agents, CMC and PSS. CMC-stabilized microspheres were larger, while PSS-stabilized microspheres were smaller and showed a slower release of AgNPs. By focusing on the development of an absorbent film embedded with biogenic vaterite $CaCO_3$−Ag microspheres, this research has shed light on various aspects, including the impact on physical, chemical, and nanomechanical properties of PVA films. The structural and spectroscopic analyses highlighted the interplay between the metallic and ionic states of silver within the vaterite $CaCO_3$−Ag system as well as the subsequent transformation upon integration into the PVA matrix. Furthermore, the reduced modulus and hardness of PVA/$CaCO_3$−Ag films exhibited significant improvement to 14.62 ± 5.23 and 0.64 ± 0.29 GPa, respectively. Importantly, the resulting films demonstrated antimicrobial activity against Gram-negative *E. coli* bacteria, affirming their potential for infection control. The investigation of AgNP release under simulated wound pH 6 conditions revealed the influence of capping agents and the PVA polymer on release behavior. Moreover, the biocompatibility assessment with human dermal fibroblast cells confirmed the safety of these films at ≤5 mg/mL concentrations. However, further investigations, such as immunogenicity assessments, are essential for future research in this field. This study reveals the interrelation and the influence of various properties, such as antimicrobial activity, crystallinity, water absorption, Ag-ion release, mechanical properties, and cell viabilities, in wound dressing films. For instance, crystallinity can impact the film's mechanical properties, including strength and elasticity. The size of vaterite $CaCO_3$−Ag microspheres can influence water absorption and the loading efficiency (LE) of AgNPs, both of which can affect cell viability. In essence, incorporating vaterite $CaCO_3$−Ag microspheres into PVA films presents a versatile strategy, yielding wound dressings that are antimicrobial, mechanically resilient, and biocompatible. The study results emphasize the significant potential of the developed films for wound dressing applications, as enhancements in crystallinity, mechanical strength, antimicrobial activity, thermal stability, and biocompatibility underline their effectiveness in addressing infection control and patient comfort.

AUTHOR INFORMATION

Corresponding Author

Wimonlak Sutapun − *Research Center for Biocomposite Materials for Medical, Agricultural and Food Industry, Suranaree University of Technology, Nakhon Ratchasima 30000, Thailand; School of Polymer Engineering, Suranaree University of Technology, Nakhon Ratchasima 30000, Thailand;* orcid.org/0000-0003-3008-8085; Email: wimonlak@sut.ac.th

Authors

Mohammad Hossein Azarian − *Research Center for Biocomposite Materials for Medical, Agricultural and Food Industry, Suranaree University of Technology, Nakhon Ratchasima 30000, Thailand;* orcid.org/0000-0003-3032-3508

Tiraporn Junyusen − *School of Agricultural Engineering, Institute of Engineering, Suranaree University of Technology, Nakhon Ratchasima 30000, Thailand*

Complete contact information is available at: https://pubs.acs.org/10.1021/acsomega.3c07135

Notes

The authors declare no competing financial interest.

ACKNOWLEDGMENTS

This work was supported by the Suranaree University of Technology (SUT), the Thailand Science Research and Innovation (TSRI), and the National Science, Research, and Innovation Fund (NSRF) via the Program Management Unit for Human Resources & Institutional Development, Research and Innovation (PMU-B) (grant number B13F660067) and via the Fundamental Fund (NRIIS number 160344). The authors would like to acknowledge Synchrotron Light Research Institute (SLRI) Thailand for conducting XPS analysis.

REFERENCES

(1) Finnegan, S.; Percival, S. L. Clinical and Antibiofilm Efficacy of Antimicrobial Hydrogels. *Adv. Wound Care* **2015**, *4* (7), 398−406.

(2) Ventola, C. L. The Antibiotic Resistance Crisis: Part 1: Causes and Threats. *J. Formul. Manage.* **2015**, *40* (5), 344−352.

(3) Sirelkhatim, A.; Mahmud, S.; Seeni, A.; Kaus, N. H. M.; Ann, L. C.; Bakhori, S. K. M.; Hasan, H.; Mohamad, D. Review on Zinc Oxide Nanoparticles: Antibacterial Activity and Toxicity Mechanism. *Nano-Micro Lett.* **2015**, *7* (3), 219−242.

(4) Wahab, R.; Mishra, A.; Yun, S. Il.; Kim, Y. S.; Shin, H. S. Antibacterial Activity of ZnO Nanoparticles Prepared via Non-Hydrolytic Solution Route. *Appl. Microbiol. Biotechnol.* **2010**, *87* (5), 1917−1925.

(5) Prabhu, S.; Poulose, E. K. Silver Nanoparticles: Mechanism of Antimicrobial Action, Synthesis, Medical Applications, and Toxicity Effects. *Int. Nano Lett.* **2012**, *2* (1), No. 32.

(6) Abd El-Mohdy, H. L. Radiation Synthesis of Nanosilver/Poly Vinyl Alcohol/Cellulose Acetate/Gelatin Hydrogels for Wound Dressing. *J. Polym. Res.* **2013**, *20* (6), No. 177, DOI: 10.1007/s10965-013-0177-6.

(7) Shamaila, S.; Zafar, N.; Riaz, S.; Sharif, R.; Nazir, J.; Naseem, S. Gold Nanoparticles: An Efficient Antimicrobial Agent against Enteric Bacterial Human Pathogen. *Nanomaterials* **2016**, *6* (4), No. 71.

(8) Pulit-Prociak, J.; Staroń, A.; Staroń, P.; Chmielowiec-Korzeniowska, A.; Drabik, A.; Tymczyna, L.; Banach, M. Preparation and of PVA-Based Compositions with Embedded Silver, Copper and

Zinc Oxide Nanoparticles and Assessment of Their Antibacterial Properties. *J. Nanobiotechnol.* **2020**, *18* (1), No. 148.
(9) Chen, H.-f.; Wu, J.; Wu, M.; Jia, H. Preparation and Antibacterial Activities of Copper Nanoparticles Encapsulated by Carbon. *New Carbon Mater.* **2019**, *34* (4), 382−389.
(10) Usman, M. S.; El Zowalaty, M. E.; Shameli, K.; Zainuddin, N.; Salama, M.; Ibrahim, N. A. Synthesis, Characterization, and Antimicrobial Properties of Copper Nanoparticles. *Int. J. Nanomed.* **2013**, *8*, 4467−4479.
(11) Yang, K.; Han, Q.; Chen, B.; Zheng, Y.; Zhang, K.; Li, Q.; Wang, J. Antimicrobial Hydrogels: Promising Materials for Medical Application. *Int. J. Nanomed.* **2018**, *13*, 2217−2263.
(12) Sánchez-López, E.; Gomes, D.; Esteruelas, G.; Bonilla, L.; Lopez-Machado, A. L.; Galindo, R.; Cano, A.; Espina, M.; Ettcheto, M.; Camins, A.; Silva, A. M.; Durazzo, A.; Santini, A.; Garcia, M. L.; Souto, E. B. Metal-Based Nanoparticles as Antimicrobial Agents: An Overview. *Nanomaterials* **2020**, *10* (2), No. 292.
(13) Shalumon, K. T.; Anulekha, K. H.; Nair, S. V.; Nair, S. V.; Chennazhi, K. P.; Jayakumar, R. Sodium Alginate/Poly(Vinyl Alcohol)/Nano ZnO Composite Nanofibers for Antibacterial Wound Dressings. *Int. J. Biol. Macromol.* **2011**, *49* (3), 247−254.
(14) Jin, G.; Prabhakaran, M. P.; Nadappuram, B. P.; Singh, G.; Kai, D.; Ramakrishna, S. Electrospun Poly(L-Lactic Acid)-Co-Poly(ϵ-Caprolactone) Nanofibres Containing Silver Nanoparticles for Skin-Tissue Engineering. *J. Biomater. Sci., Polym. Ed.* **2012**, *23* (18), 2337−2352.
(15) Rybka, M.; Mazurek, Ł.; Konop, M. Beneficial Effect of Wound Dressings Containing Silver and Silver Nanoparticles in Wound Healing—From Experimental Studies to Clinical Practice. *Life* **2023**, *13* (1), No. 69.
(16) 3M Tegaderm Ag Mesh Dressing with Silver. https://www.3m.com/3M/en_US/p/d/b00036068/.
(17) AQUACEL Ag SURGICAL cover dressing. https://www.convatec.com/products/advanced-wound-care/wound-type/pc-wound-closed-surgical-solutions/aquacel-ag-surgical-cover-dressing/.
(18) ACTICOAT Antimicrobial Barrier Silver Dressings. https://educationunlimited.smith-nephew.com/enrol/index.php?id=168.
(19) Ueda, M.; Yokota, T.; Honda, M.; Lim, P. N.; Osaka, N.; Makita, M.; Nishikawa, Y.; Kasuga, T.; Aizawa, M. Regulating Size of Silver Nanoparticles on Calcium Carbonate via Ultrasonic Spray for Effective Antibacterial Efficacy and Sustained Release. *Mater. Sci. Eng. C* **2021**, *125*, 112083.
(20) Azarian, M. H.; Sutapun, W. Biogenic Calcium Carbonate Derived from Waste Shells for Advanced Material Applications: A Review. *Front. Mater.* **2022**, *9*, No. 1024977.
(21) Zin, M. E. E.; Moolkaew, P.; Junyusen, T.; Sutapun, W. Preparation of Hybrid Particles of Ag Nanoparticles and Eggshell Calcium Carbonate and Their Antimicrobial Efficiency against Beef-Extracted Bacteria. *R. Soc. Open Sci.* **2023**, *10* (5), No. 221197, DOI: 10.1098/rsos.221197.
(22) Azarian, M. H.; Sutapun, W. Tuning Polymorphs of Precipitated Calcium Carbonate from Discarded Eggshells: Effects of Polyelectrolyte and Salt Concentration. *RSC Adv.* **2022**, *12* (23), 14729−14739.
(23) Lauth, V.; Loretz, B.; Lehr, C. M.; Maas, M.; Rezwan, K. Self-Assembly and Shape Control of Hybrid Nanocarriers Based on Calcium Carbonate and Carbon Nanodots. *Chem. Mater.* **2016**, *28* (11), 3796−3803.
(24) Lauth, V.; Maas, M.; Rezwan, K. An Evaluation of Colloidal and Crystalline Properties of CaCO3 Nanoparticles for Biological Applications. *Mater. Sci. Eng.: C* **2017**, *78*, 305−314.
(25) Tottoli, E. M.; Dorati, R.; Genta, I.; Chiesa, E.; Pisani, S.; Conti, B. Skin Wound Healing Process and New Emerging Technologies for Skin Wound Care and Regeneration. *Pharmaceutics* **2020**, *12* (8), No. 735.
(26) Mortier, C.; Costa, D. C. S.; Oliveira, M. B.; Haugen, H. J.; Lyngstadaas, S. P.; Blaker, J. J.; Mano, J. F. Advanced Hydrogels Based on Natural Macromolecules: Chemical Routes to Achieve Mechanical Versatility. *Mater. Today Chem.* **2022**, *26*, No. 101222.
(27) Arkaban, H.; Barani, M.; Akbarizadeh, M. R.; Chauhan, N. P. S.; Jadoun, S.; Soltani, M. D.; Zarrintaj, P. Polyacrylic Acid Nanoplatforms: Antimicrobial, Tissue Engineering, and Cancer Theranostic Applications. *Polymers* **2022**, *14* (6), No. 1259.
(28) Geng, H.; Zhang, P.; Liu, L.; Shangguan, Y.; Cheng, X.; Liu, H.; Zhao, Y.; Hao, J.; Li, W.; C, J. Convergent Architecting of Multifunction-in-One Hydrogels as Wound Dressings for Surgical Anti-Infections. *Mater. Today Chem.* **2022**, *25*, No. 100968.
(29) Rodríguez-Vázquez, M.; Vega-Ruiz, B.; Ramos-Zúñiga, R.; Saldaña-Koppel, D. A.; Quiñones-Olvera, L. F. Chitosan and Its Potential Use as a Scaffold for Tissue Engineering in Regenerative Medicine. *BioMed Res. Int.* **2015**, *2015*, No. 821279.
(30) Lopes, M. S.; Jardini, A. L.; Filho, R. M. Poly (Lactic Acid) Production for Tissue Engineering Applications. *Procedia Eng.* **2012**, *42*, 1402−1413.
(31) Cen, L.; Liu, W.; Cui, L.; Zhang, W.; Cao, Y. Collagen Tissue Engineering: Development of Novel Biomaterials and Applications. *Pediatr. Res.* **2008**, *63* (5), 492−496.
(32) Chircov, C.; Grumezescu, A. M.; Bejenaru, L. E. Hyaluronic Acid-Based Scaffolds for Tissue Engineering. *Rom. J. Morphol. Embryol.* **2018**, *59* (1), 71−76.
(33) Su, K.; Wang, C. Recent Advances in the Use of Gelatin in Biomedical Research. *Biotechnol. Lett.* **2015**, *37* (11), 2139−2145.
(34) Malikmammadov, E.; Tanir, T. E.; Kiziltay, A.; Hasirci, V.; Hasirci, N. PCL and PCL-Based Materials in Biomedical Applications. *J. Biomater. Sci., Polym. Ed.* **2018**, *29* (7−9), 863−893.
(35) Azarian, M. H.; Boochathum, P.; Kongsema, M. Biocompatibility and Biodegradability of Filler Encapsulated Chloroacetated Natural Rubber/Polyvinyl Alcohol Nanofiber for Wound Dressing. *Mater. Sci. Eng.: C* **2019**, *103*, No. 109829.
(36) Azarian, M. H.; Boochathum, P. Nanofiber Films of Chloroacetated Natural Rubber/Poly (Vinyl Alcohol) by Electrospinning Technique: Silica Effects on Biodegradation. *J. Appl. Polym. Sci.* **2018**, *135*, No. 46432.
(37) Kumar, A.; Han, S. S. PVA-Based Hydrogels for Tissue Engineering: A Review. *Int. J. Polym. Mater. Polym. Biomater.* **2017**, *66* (4), 159−182.
(38) Song, S.; Liu, Z.; Abubaker, M. A.; Ding, L.; Zhang, J.; Yang, S.; Fan, Z. Antibacterial Polyvinyl Alcohol/Bacterial Cellulose/Nano-Silver Hydrogels That Effectively Promote Wound Healing. *Mater. Sci. Eng.: C* **2021**, *126*, No. 112171.
(39) Jiang, S.; Liu, S.; Feng, W. PVA Hydrogel Properties for Biomedical Application. *J. Mech. Behav. Biomed. Mater.* **2011**, *4* (7), 1228−1233.
(40) Augustine, R.; Hasan, A.; Nath, V. K. Y.; Thomas, J.; Augustine, A.; Kalarikkal, N.; Al Moustafa, A.-E.; Thomas, S. Electrospun Polyvinyl Alcohol Membranes Incorporated with Green Synthesized Silver Nanoparticles for Wound Dressing Applications. *J. Mater. Sci.: Mater. Med.* **2018**, *29* (11), 163.
(41) Guo, Y.; Xu, L.; Chen, K. Preparation and Properties of Silver-Loaded PVA/CS/Gel Hydrogel Wound Dressing. *Soft Mater.* **2023**, *21* (1), 92−101.
(42) Kontoyannis, C. G.; Vagenas, N. V. Calcium Carbonate Phase Analysis Using XRD and FT-Raman Spectroscopy. *Analyst* **2000**, *125* (2), 251−255.
(43) Mahmood, W. A. K.; Azarian, M. H.; bt Wan Fathilah, W. F.; Kwok, E. Nanoencapsulation of MMT Clay within Polyethylene Glycol (PEG) Nano-Beads by Electrospraying. *J. Appl. Polym. Sci.* **2017**, *134*, No. 45048.
(44) Guirguis, O. W.; Moselhey, M. T. H. Thermal and Structural Studies of Poly (Vinyl Alcohol) and Hydroxypropyl Cellulose Blends. *Nat. Sci.* **2012**, *04* (01), 57−67.
(45) Weng, S.; Zhao, X.; Liu, G.; Guan, Y.; Wu, F.; Luo, Y. Synthesis, Characterization, Antibacterial Activity in Dark and in Vitro Cytocompatibility of Ag-Incorporated TiO2Microspheres with High Specific Surface Area. *J. Mater. Sci.: Mater. Med.* **2018**, *29* (5), No. 50, DOI: 10.1007/s10856-018-6042-8.
(46) Ferreira, A. M.; Vikulina, A.; Cave, G. W. V.; Loughlin, M.; Puddu, V.; Volodkin, D. Vaterite-Nanosilver Hybrids with Antibacterial

Properties and PH-Triggered Release. *Mater. Today Chem.* **2023**, *30*, No. 101586.
(47) Jahani, D.; Nazari, A.; Ghourbanpour, J.; Ameli, A. Polyvinyl Alcohol/Calcium Carbonate Nanocomposites as Efficient and Cost-Effective Cationic Dye Adsorbents. *Polymers* **2020**, *12* (10), No. 2179.
(48) Aziz, S. B.; Abdullah, O. G.; Hussein, S. A.; Ahmed, H. M. Effect of PVA Blending on Structural and Ion Transport Properties of CS:AgNt-Based Polymer Electrolyte Membrane. *Polymers* **2017**, *9* (11), No. 622.
(49) Azarian, M. H.; Mahmood, W. A. K.; Kwok, E.; Bt Wan Fathilah, W. F.; Ibrahim, N. F. B. Nanoencapsulation of Intercalated Montmorillonite-Urea within PVA Nanofibers: Hydrogel Fertilizer Nanocomposite. *J. Appl. Polym. Sci.* **2018**, *135* (10), No. 45957.
(50) Xu, S.; Zhang, F.; Song, J.; Kishimoto, Y.; Morikawa, H. Preparation of Silver Nanoparticle-Coated Calcium Alginate Fibers by Hyperbranched Poly(Amidoamine)-Mediated Assembly and Their Antibacterial Activity. *Text. Res. J.* **2016**, *86* (8), 878−886.
(51) Uznanski, P.; Zakrzewska, J.; Favier, F.; Kazmierski, S.; Bryszewska, E. Synthesis and Characterization of Silver Nanoparticles from (Bis)Alkylamine Silver Carboxylate Precursors. *J. Nanopart. Res.* **2017**, *19* (3), No. 121, DOI: 10.1007/s11051-017-3827-5.
(52) Jiménez, J. A.; Liu, H.; Fachini, E. X-Ray Photoelectron Spectroscopy of Silver Nanoparticles in Phosphate Glass. *Mater. Lett.* **2010**, *64* (19), 2046−2048.
(53) Kumari, P.; Majewski, P. Adsorption of Albumin on Silica Surfaces Modified by Silver and Copper Nanoparticles. *J. Nanomater.* **2013**, *2013*, No. 6.
(54) Mohamedkhair, A. K.; Drmosh, Q. A.; Yamani, Z. H. Silver Nanoparticle-Decorated Tin Oxide Thin Films: Synthesis, Characterization, and Hydrogen Gas Sensing. *Front. Mater.* **2019**, *6*, No. 188.
(55) Butler, J.; Handy, R. D.; Upton, M.; Besinis, A. Review of Antimicrobial Nanocoatings in Medicine and Dentistry: Mechanisms of Action, Biocompatibility Performance, Safety, and Benefits Compared to Antibiotics. *ACS Nano* **2023**, *17* (8), 7064−7092.
(56) Yang, H.; Xu, S.; Jiang, L.; Dan, Y. Thermal Decomposition Behavior of Poly (Vinyl Alcohol) with Different Hydroxyl Content. *J. Macromol. Sci., Part B* **2012**, *51* (3), 464−480.
(57) Holland, B. J.; Hay, J. N. The Thermal Degradation of Poly(Vinyl Alcohol). *Polymer* **2001**, *42* (16), 6775−6783.
(58) Bilton, M.; Brown, A. P.; Milne, S. J. Investigating the Optimum Conditions for the Formation of Calcium Oxide, Used for CO 2 Sequestration, by Thermal Decomposition of Calcium Acetate. *J. Phys.: Conf. Ser.* **2012**, *371*, No. 012075.
(59) Safandowska, M.; Makarewicz, C.; Rozanski, A.; Idczak, R. Barrier Properties of Semicrystalline Polylactide: The Role of the Density of the Amorphous Regions. *Macromolecules* **2022**, *55*, 10077−10089.
(60) Moshtagh, P. R.; Rauker, J.; Sandker, M. J.; Zuiddam, M. R.; Dirne, F. W. A.; Klijnstra, E.; Duque, L.; Steendam, R.; Weinans, H.; Zadpoor, A. A. Nanomechanical Properties of Multi-Block Copolymer Microspheres for Drug Delivery Applications. *J. Mech. Behav. Biomed. Mater.* **2014**, *34*, 313−319.
(61) Shemesh, M.; Zilberman, M. Structure−Property Effects of Novel Bioresorbable Hybrid Structures with Controlled Release of Analgesic Drugs for Wound Healing Applications. *Acta Biomater.* **2014**, *10* (3), 1380−1391.
(62) Aderibigbe, B. A. Hybrid-Based Wound Dressings: Combination of Synthetic and Biopolymers. *Polymers* **2022**, *14* (18), No. 3806.
(63) Satyavani, K.; Gurudeeban, S.; Ramanathan, T.; Balasubramanian, T. Toxicity Study of Silver Nanoparticles Synthesized from Suaeda Monoica on Hep-2 Cell Line. *Avicenna J. Med. Biotechnol.* **2012**, *4* (1), 35−39.
(64) Pencheva, D.; Bryaskova, R.; Kantardjiev, T. Polyvinyl Alcohol/Silver Nanoparticles (PVA/AgNps) as a Model for Testing the Biological Activity of Hybrid Materials with Included Silver Nanoparticles. *Mater. Sci. Eng.: C* **2012**, *32* (7), 2048−2051.
(65) Eghbalifam, N.; Frounchi, M.; Dadbin, S. Antibacterial Silver Nanoparticles in Polyvinyl Alcohol/Sodium Alginate Blend Produced by Gamma Irradiation. *Int. J. Biol. Macromol.* **2015**, *80*, 170−176.
(66) Tripathi, R. M.; Pudake, R. N.; Shrivastav, B. R.; Shrivastav, A. Antibacterial Activity of Poly (Vinyl Alcohol)—Biogenic Silver Nanocomposite Film for Food Packaging Material. *Adv. Nat. Sci.: Nanosci. Nanotechnol.* **2018**, *9* (2), No. 025020.
(67) Abdelrahman, T.; Newton, H. Wound Dressings: Principles and Practice. *Surgery* **2011**, *29* (10), 491−495.
(68) Nguyen, H. M.; Le, T. T. N.; Nguyen, A. T.; Le, H. N. T.; Pham, T. T. Biomedical Materials for Wound Dressing: Recent Advances and Applications. *RSC Adv.* **2023**, *13* (8), 5509−5528.

https://doi.org/10.1021/acsomega.3c07135
ACS Omega 2024, 9, 955−969